

Precision assessment of label-free psoriasis biomarkers with ultra-broadband optoacoustic mesoscopy

Juan Aguirre¹, Mathias Schwarz¹, Natalie Garzorz^{2,3}, Murad Omar¹, Andreas Buehler¹, Kilian Eyerich^{2,3} and Vasilis Ntziachristos^{1*}

Imaging plays a critical role in the diagnosis and assessment of dermatological conditions. However, optical or optoacoustic microscopy techniques are limited to visualizing superficial skin features owing to strong photon scattering, whereas ultrasound methods, which can probe deeper-seated tissue, lack the contrast to image pathophysiological mechanisms in detail. Here, we demonstrate that raster-scan optoacoustic mesoscopy (RSOM) implemented in ultra-broadband (10–180 MHz) detection mode bridges the depth capabilities of ultrasound and the resolution range and high contrast of optical methods in clinical dermatology. Using tomographic reconstruction and frequency equalization to represent low and high spatial-frequency components, we visualize skin morphology and vascular patterns in the dermis and sub-dermis of psoriasis patients, enabling quantification of inflammation and other biomarkers of psoriasis without the need for contrast agents. Implemented in a hand-held device, we showcase how label-free biomarkers detected by RSOM correlate with clinical score. The method can also be extended to assess a larger spectrum of dermatological conditions.

Psoriasis is a chronic inflammatory skin disease with adverse effects on quality of life and the socioeconomic system^{1,2}. Current progress in understanding the pathogenesis reveals that immune dysregulation of T helper 17 cells results in a hyper-proliferative and metabolically activated epidermis³, manifested as red patches with silver scales. The disease phenotype comprises an increase in the mitotic rate of keratinocytes, thickening of the stratum spinosum (acanthosis) and strong inflammatory cellular infiltrate consisting of T cells, macrophages and dendritic cells¹. Moreover, the dermal areas of psoriatic skin are marked by increased vascularization and an increase of tortuous capillaries in the upper dermis^{1,4}. Nevertheless, many aspects of the psoriasis pathogenesis remain poorly understood. Moreover, lack of biomarkers and objective methods to phenotype the heterogeneous presentation of psoriasis challenges prediction of a therapeutic strategy outcome for individual patients³.

Psoriatic skin is clinically assessed using the Psoriasis Area Severity Index (PASI)⁵, calculated by scoring the appearance of lesion redness, plaque thickness, scaling and percentage of the body affected. PASI is nevertheless subjective and does not assess subsurface features, such as general morphology, vasculature or angiogenesis^{6,7}, even though the release of growth factors (vascular endothelial growth factor, epidermal growth factors, transforming growth factor beta) and changes in vascular architecture are identified as a major hallmark of psoriatic inflammation and typically associated with disease progression^{4,8}.

Confocal or two-photon microscopy have been considered for skin visualization but they only assess depths of a few hundred micrometres, which is not appropriate for the thickened psoriatic epidermis^{9,10}. Optical coherence tomography can provide skin morphology images at depths of 1–2 mm using near-infrared light

(~1,300 nm)^{11,12}, but imaging of vascular networks observed using flow-sensitive techniques in the visible range^{13,14} is limited to depths of ~400 µm¹⁵. Moreover, inherent image artefacts in the axial direction have not yet been addressed and compromise the ability of optical coherence tomography to obtain cross-sectional images. As an alternative, high-frequency ultrasound penetrates several millimetres into skin tissue. However, the resulting images exhibit pronounced speckle effects and do not visualize vessels of <100 µm in diameter, unless contrast agents (microbubbles) are employed¹⁶, imposing limitations for routine longitudinal applications in humans. Moreover, ultrasonic contrast has reduced sensitivity to changes associated with pathophysiology, inflammation and angiogenesis¹⁷. Therefore, studies of subsurface skin pathophysiology and longitudinal observations are limited by the *in vivo* imaging tools available today^{8,9}.

We present a different approach to skin imaging by developing a system for portable ultra-broadband (10–180 MHz) raster-scan optoacoustic mesoscopy (UB-RSOM), and investigate how the imaging features associated with psoriasis and other dermatological conditions relate to pathophysiological metrics of disease. Conventional ultrasound and optoacoustic imaging use frequencies within a narrow band (for example, 5–20 MHz), which defines the resolution range and overall image quality achieved. Conversely, UB-RSOM implements ultra-short photon pulses (<2 ns) that excite an ultra-broad ultrasound frequency spectrum. Central to achieving high-performance ultra-broadband imaging is the use of a spherically focused transducer constructed using a lithium niobate crystal (LiNbO₃) for detection of optoacoustic signals at high numerical apertures (>60°) and a detection-frequency range of 10–180 MHz (that is, bandwidth=170 MHz). We investigated features offered by UB-RSOM in healthy and diseased skin, and

¹Technische Universität München and Institute for Biological and Medical Imaging, Helmholtz Zentrum München, Ingolstädter Landstrasse 1, D85764 Neuherberg, Germany. ²Department of Dermatology and Allergy, Technical University of Munich, 80802 Munich, Germany. ³Center for Allergy and Environment (ZAUM), Technical University of Munich and Helmholtz Center Munich, 80802 Munich, Germany. *e-mail: v.ntziachristos@tum.de

developed frequency band equalization (FBE) to effectively utilize the broad frequency content. We demonstrate the visualization of pathophysiological skin features *in vivo* in label-free mode, which has not been achieved by other imaging modalities. We show how tomographic reconstruction of absorption contrast can quantify critical dermatological sub-surface features associated with dermal angiogenesis and skin inflammation, without using contrast agents, and demonstrate the highest resolution-to-depth ratio yet reported for the label-free mode. We devise a UB-RSOM index for skin conditions aiming to offer a quantitative metric of disease severity in the context of precision medicine requirements, and then compare it to clinical score. Finally, we discuss how the method can advance the study and quantification of dermatological conditions and their response to treatment.

Results

Qualitative evaluation of the skin-imaging performance of optoacoustic mesoscopy. Developed for portable skin imaging (see Fig. 1a–c and Methods), UB-RSOM conforms to the human-use safety limits described in the *American National Standard for Safe Use of Lasers* (ANSI Z136.1-2014, Laser Institute of America; see Methods). Handheld operation was achieved by designing a compact scan head (see Methods) that employed fixed illumination to overcome image artefacts arising from spatially dependent optical-fluence variations common to raster-scan implementations that move in tandem with both the sound detector and the illuminator¹⁸.

Detected signals were reconstructed and were separated into two frequency bands, typically 10–60 MHz (Fig. 1d) and 60–180 MHz (Fig. 1e); or alternatively, 10–42 MHz and 42–120 MHz bands (see Methods and Supplementary Fig. 1). A low-frequency band image (rendered in red) and a high-frequency band image (rendered in green) were correspondingly reconstructed, frequency equalized (see Methods) and co-registered (Fig. 1d–f). This operation allows rendering of fine spatial details together with lower-resolution skin structures, which are typically of higher intensity. Images from healthy volunteers were collected from areas spanning 8 mm × 2 mm (scan time, 80 s) to 8 mm × 8 mm (scan time, 320 s).

Cross-sectional skin images (Fig. 1f) revealed the epidermis, dermis, capillary loops and the horizontal plexus of the dermis (see Supplementary Note 1 for skin-layer representation). These images reached a depth of ~1.5 mm for the 532 nm illumination shown in Fig. 1, and ~5 mm for near-infrared light. Coronal plots of the three-dimensional images depict the superficial skin ridges of the epidermal layer (Fig. 1g), a top-down view of the capillary loops in green (Fig. 1h) and the dermal vasculature in the vascular plexus (Fig. 1i).

The superiority of ultra-broadband detection is shown by contrasting UB-RSOM images with those obtained via conventional optoacoustic imaging whose bandwidth is a few tens of megahertz (see Supplementary Note 2). Even compared with a wide 10–40 MHz range, the UB-RSOM resolution is over eight times greater (Supplementary Fig. 2). Consequently, Fig. 1f–i shows non-invasive imaging of dermal vasculature, skin layers and capillary loops at a level of detail and a resolution-to-depth ratio that has not been achieved by other modalities. The combination of ultra-broad bandwidth and frequency equalization therefore brings never-before-documented capabilities to skin imaging.

UB-RSOM of psoriasis and histological validation. The next step was to investigate whether UB-RSOM could resolve and quantify features of psoriasis. Affected skin areas measuring 4 mm × 2 mm from six psoriasis patients (see Methods) were imaged (Fig. 2a), revealing marked changes compared with healthy skin (Fig. 2b). The scan time was 70 s. Elongated and dilated capillary loops, visualized in green via FBE (equation (2)), could clearly be seen climbing through the rete ridges almost up to the skin surface. The

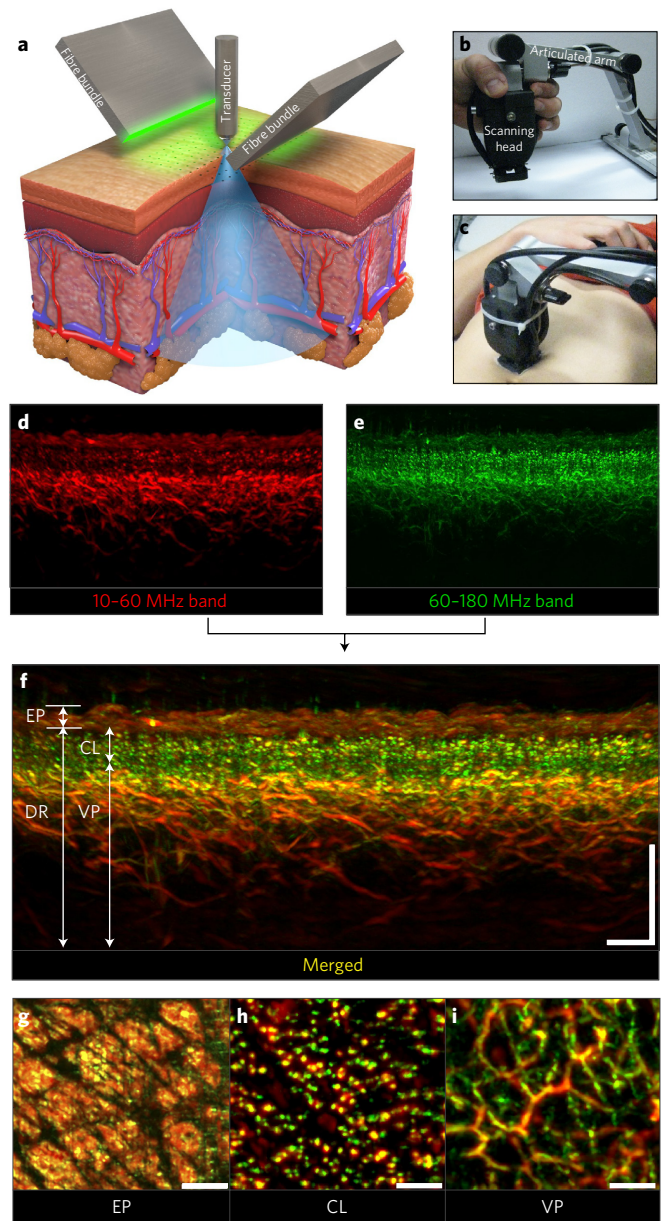


Figure 1 | Skin imaging with the portable UB-RSOM system, using colour coding of frequency bands. **a**, Schematic of the operation of UB-RSOM. The transducer is raster-scanned parallel to the skin surface, acquiring acoustic signals (A lines) that are generated by laser illumination from two fixed fibre bundles. The focal point of the transducer is kept above the skin surface. **b**, Photograph of the scanning head and the articulated arm. **c**, Photograph of the scanning head in position, ready for data acquisition. **d,e**, The collected optoacoustic signals are filtered in two frequency bands and reconstructed into two images shown in red and green, representing low and high spatial frequencies, respectively. **f**, UB-RSOM image of healthy skin, generated by the FBE method (equation (2)), which combines low and high spatial frequencies in a single colour-coded image. Different biological structures appear in red or green depending on their spatial frequency. The epidermis (EP) appeared mostly in red, and could be clearly distinguished from the dermis (DR). In the dermal vasculature, the capillary loops (CL) could be distinguished from the epidermis and from the vascular plexus (VP) in the deep dermis. The larger vessels appeared mainly in red, whereas the smaller vessels appeared mainly in green. **g–i**, Maximum intensity projections in the coronal direction of the epidermis, showing the indentations of the skin (**g**), the capillary loop layer (**h**) and the dermis (**i**). All scale bars, 500 μ m.

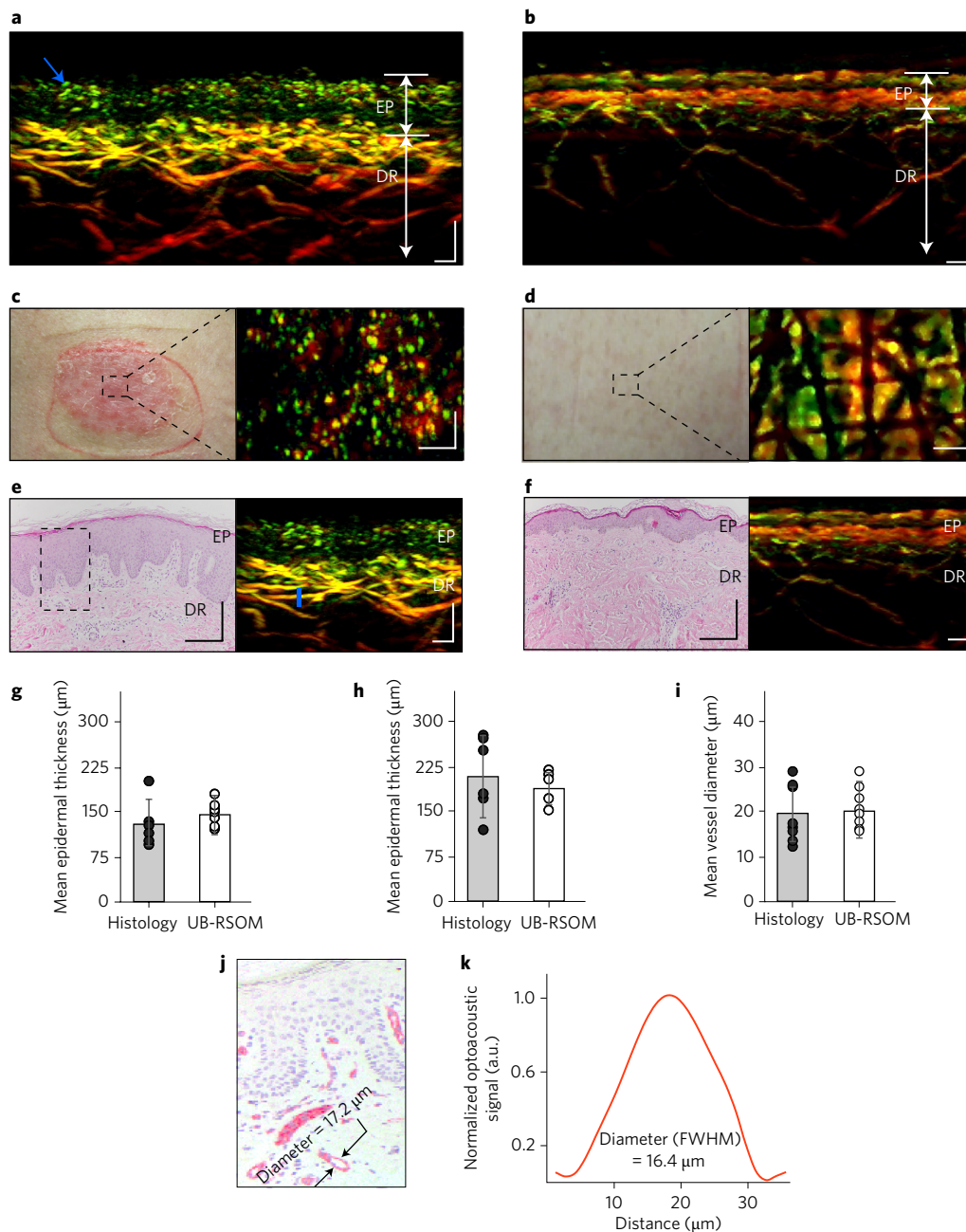


Figure 2 | UB-RSOM of healthy skin versus adjacent psoriatic skin and validation by histology. **a**, UB-RSOM cross-sectional image of psoriatic skin showing the top part of elongated capillary loops (blue arrow) that almost climbed to the skin surface through elongated rete ridges. The capillaries appeared in green (due to FBE processing), interleaved with widened epidermal structures (EP) that were the result of acanthosis. These structures appeared in red with poor contrast due to loss of pigmentation. Below the epidermis, a dilated and dense vascular structure of the dermis (DR) is resolved (in red). Capillary loops were observed in green and separated from the epidermis (red) and the dilated dermal vasculature (red). Scale bars, 200 μm . **b**, UB-RSOM cross-sectional image of adjacent healthy skin showing a layered epidermal structure (EP) with clearly resolved vessels in the dermis (DR). Scale bars, 200 μm . **c**, Photograph of the top of the psoriatic skin region (left) encompassing an area (dashed box) from which the coronal UB-RSOM slice of the epidermal region was taken (right). The top of the capillary loops appear clearly as green dots. Scale bars, 300 μm . **d**, Photograph of the top of the healthy skin region (left). In the corresponding UB-RSOM coronal view, the superficial skin indentations are visible. Scale bars, 300 μm . **e**, Histology image (left) of the psoriatic skin and the corresponding UB-RSOM cross-sectional image (right). The histology image shows the acanthosis, the elongated capillary loops through the rete ridge and the increased vascularization of the dermis. Scale bars, 200 μm . **f**, Histology image (left) of healthy skin and the corresponding UB-RSOM cross-sectional image (right). Scale bars, 200 μm . **g**, Epidermal thickness of healthy skin measured from the UB-RSOM and histology images. $n = 6$, obtained from a representative patient. **h**, Epidermal thickness of psoriatic skin measured from the UB-RSOM and histology images. $n = 6$, obtained from a representative patient. **i**, Vessel diameters in psoriatic skin measured from the UB-RSOM and CD31 immunostaining images. $n = 9$, obtained from a representative patient. Error bars represent the standard deviation and the circles represent the individual measurements. **j**, CD31 immunostaining of psoriatic skin (dashed rectangle in **e**), from which the diameter of a vessel in the dermis well below the capillary loops was measured. **k**, Optoacoustic profile (cross-section corresponding to the blue line in **e**) of a vessel parallel to the psoriatic skin surface situated in the dermis, well below the capillary loops. The vessel diameter was calculated as the full width at half maximum (FWHM) of the optoacoustic signal.

layered arrangement observed in the healthy skin disappears in psoriasis and prominent skin acanthosis could be measured by observing the distance from the skin surface to the horizontal vascular plexus. Compared with the healthy skin, dermal vessels had larger diameters and were denser in appearance; this can also be seen in the three-dimensional skin visualizations shown in Supplementary Video 1 (healthy) and Supplementary Video 2 (psoriatic). Coronal UB-RSOM images close to the surface of the psoriatic skin, showing the tops of the capillary loops (Fig. 2c), were markedly different to the corresponding images of healthy skin (Fig. 2d). Histological haematoxylin and eosin analysis of biopsied specimens were compared with the corresponding UB-RSOM cross-sections for psoriatic and healthy skin (Fig. 2e,f). The histological specimens confirmed the epidermal thickening, capillary elongation and increased dermal vascularization that was visualized by the label-free UB-RSOM *in vivo*. Quantitative comparison (see Methods) of the mean epidermal thicknesses that were observed in the UB-RSOM and histological images showed a good match between the two methods; for both the healthy ($\sim 138\ \mu\text{m}$) and psoriatic ($\sim 203\ \mu\text{m}$) epidermal thickness (Fig. 2g,h). An excellent match was found between the histologically determined diameter of individual vessels in the deep dermis (visualized using CD31 immunostaining; $n=9$) and the corresponding value determined from UB-RSOM images (Fig. 2i–k).

Calculation of UB-RSOM vascular and epidermal features in psoriatic patients and their clinical relevance. Cross-sectional images from different patients revealed marked differences in disease manifestation (Fig. 3a,b). The next goal of the study was therefore to quantify pathophysiological features of psoriasis appearing in the study group. UB-RSOM cross-sectional images and three-dimensional reconstructions were examined for morphological skin alterations, capillary loop elongation, acanthosis and changes in dermal vasculature. We computed (1) the total blood volume (TBV) in the dermis, (2) the fractal number of the vascular structure, (3) the thickness of the epidermis, (4) the density of the capillary loops and (5) the mean diameter of the capillary loops (see Methods). These measurements were interrogated as label-free biomarkers corresponding to clinically related indications, as will be explained in the following paragraphs.

The TBV relates to the ‘flush’ of the inflammatory phenotype. TBV values were computed as the number of voxels in the dermis that corresponded to the inner lumen of blood vessels, based on image segmentation (see Methods). Each psoriatic lesion exhibited a higher TBV compared with the adjacent healthy skin. The mean TBVs for psoriatic and healthy skin were $0.11 \pm 0.02\ \text{mm}^3$ and $0.071 \pm 0.02\ \text{mm}^3$, respectively (Fig. 3c). A paired *t*-test and a Wilcoxon signed-rank test showed significant differences ($P < 0.01$ and $P < 0.05$, respectively) between the TBV in healthy skin and that in adjacent psoriatic areas. To compare areas of different sizes, we defined a metric for the blood volume per skin surface (mm): TBV per area, where ‘area’ was defined as the total area scanned by UB-RSOM.

The fractal number of the vascular structures was computed as a second label-free landmark of chronic inflammation and measures vascular spatial complexity associated with vascular changes and aberrant angiogenesis. The higher the fractal number the higher the spatial complexity¹⁹. The psoriatic skin exhibited a higher mean fractal number of 1.58 ± 0.06 arbitrary units (a.u.), compared with 1.49 ± 0.09 a.u. for healthy skin (Fig. 3c). A higher fractal number versus healthy skin was also calculated on a per lesion basis (Fig. 3c). A paired *t*-test and a Wilcoxon signed-rank test showed significant differences between the fractal number of healthy skin versus adjacent psoriatic areas ($P < 0.01$ and $P < 0.05$, respectively).

A third inflammatory landmark related to the psoriasis-associated thickness of the epidermis, which also exhibited marked differences between psoriatic and healthy skin (Fig. 3c). The mean values

for psoriatic and healthy skin were $371 \pm 102\ \mu\text{m}$ and $108 \pm 27\ \mu\text{m}$, respectively; although lesion thickness in individual patients exhibited marked differences (see Fig. 2h). The mean thickness difference (acanthosis) between psoriatic and healthy skin was $263 \pm 122\ \mu\text{m}$ (Fig. 3c). A paired *t*-test and a Wilcoxon signed-rank test showed significant differences between the thickness of the epidermis in healthy skin and that in adjacent psoriatic areas ($P < 0.01$ and $P < 0.05$, respectively).

We also analysed the appearance and density of the capillary loops, which are usually indicative of chronic inflammation and skin reconstruction. The capillary loops of the psoriatic skin were clearly detected in the 15–120 MHz window and exhibited a mean diameter of $33 \pm 4\ \mu\text{m}$ (Fig. 3d). The mean density of capillary loops in the psoriatic plaques was 21 ± 6 capillaries per mm^2 . Characteristically, the capillary loops in healthy skin have smaller diameters and they were not visible in the 15–120 MHz window, only appearing when frequencies of over 120 MHz were employed (Fig. 1f,h). This finding serves as an example of how spatial-frequency patterns can be employed to differentiate conditions and disease.

Finally we interrogated the clinical relevance of the UB-RSOM features by suggesting a new index of optoacoustic features (OPIND), which could quantitatively summarize psoriasis features and severity. OPIND was strongly correlated with the PASI index (see Fig. 3e and ‘Calculation of OPIND’ in Methods).

Discussion

In addition to measuring genomic and environmental variability, precision medicine requires methods that sense and quantify individual disease conditions and responses from patients. Effective clinical application necessitates label-free, non-invasive methods for capturing pathophysiological phenotypes. Such methods allow longitudinal investigation of the underlying biology without perturbing the disease being monitored. The combination of *ex vivo* analytics with *in vivo* measurements could lead to improved disease prevention, early diagnosis and treatment.

UB-RSOM offers an approach to quantifying skin morphology and inflammatory landmarks that is not available to other current modalities in dermatology, due to ultra-short illumination, ultra-broadband LiNbO₃ detection, and tomographic reconstruction using high-numerical aperture data collection. UB-RSOM-resolved light absorption contrast allows direct and highly sensitive detection of vascular (haemoglobin) and melanin structures, thereby imparting an alternative picture of the pathophysiology. As shown in Supplementary Note 2, the broad bandwidth is essential to the imaging performance of UB-RSOM. Optoacoustic imaging of the skin using a more limited bandwidth has been described in previous studies^{13,20}, and as shown in Supplementary Fig. 2, its resolution is above $100\ \mu\text{m}$, which is not sufficient for analysis of the fine features visualized using our system^{21–25}. Ultra-broadband detection enabled axial and lateral resolutions of $4.5\ \mu\text{m}$ and $18.4\ \mu\text{m}$, respectively, which generally remained approximately constant throughout the whole dermis (1.5 mm deep) and degraded slightly in deeper layers; for example, the lateral resolution was $\sim 23\ \mu\text{m}$ in fat-layer capillaries situated 2.5 mm below the surface (see Supplementary Note 4 for details). Repeated measurements of the same area were performed and they showed that no significant changes in the skin vascular structure were produced by illumination-induced tissue heating.

In addition to the imaging performance shown, a critical finding was the identification of skin features, which enabled not only morphological inspection but also the interrogation of inflammatory and angiogenic features not resolved by current dermatological imaging techniques. Vascularization of the dermis is suspected to play a key role in the development of psoriasis^{4,8}, but so far, it has remained invisible *in vivo*. Likewise, a larger number of disease biomarkers (epidermal thickness, blood volume density and diameter of capillary loops) were summarized into OPIND to serve as a

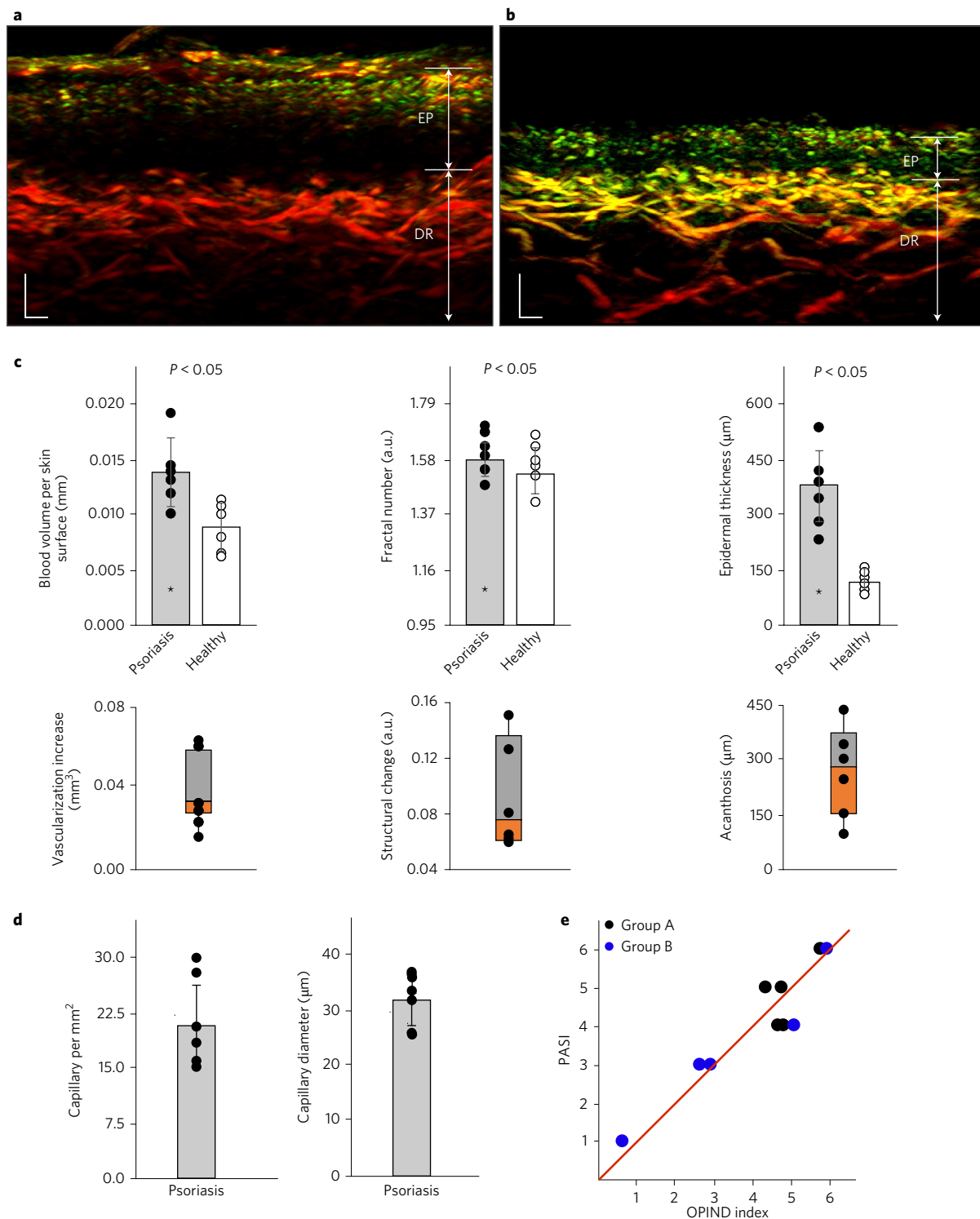


Figure 3 | Clinical relevance of UB-RSOM measurements. **a, b**, Cross-sectional UB-RSOM images of two different psoriatic patients (A6 (left) and A1 (right)). The thickness of the epidermis (EP) was significantly different for both patients. The vascular structure in the dermis (DR) shows dilated and tortuous vessels. Scale bars, 200 μm . **c**, Top: measurements of the TBV, fractal number and epidermal thickness for psoriatic and adjacent healthy skin ($n = 6$, patients A1 to A6). For each of the metrics, there were statistically significant differences between healthy and the psoriatic skin. Error bars, s.d. Bottom: box-and-whisker plots of the differences between measurements for psoriatic and healthy skin. The difference in TBV refers to increased vasculature, the difference in fractal number to structural changes, and the difference in epidermal thickness to acanthosis. The orange and grey parts, respectively, correspond to values from the median to the third quartile and values from the median to the first quartile. **d**, Quantification of the features corresponding to the capillary loops measured from the UB-RSOM images. $n = 6$; error bars, s.d. **e**, OPIND index versus PASI index for the validation dataset ($n = 5$) and the test dataset ($n = 6$). The OPIND index calculated for the group B data using the coefficients obtained from the group A data explains 96% of the variance of the corresponding PASI index. The red line represents the ideal case in which the OPIND index would exactly correspond to the PASI index.

quantitative measure of disease severity. Pilot comparison between OPIND and PASI revealed a good correlation, even though some differences between the two indices are to be expected since OPIND takes account of three-dimensional features whereas PASI only covers the surface appearance of disease. We expect that the concept of OPIND, possibly after refinement, will offer a quantitative and objective measure of inflammatory skin disease, improving on the subjective nature of PASI (or other indices such as SCORAD). The mean difference in fractal number between healthy and psoriatic skin was only 6%, indicating small changes in the pattern complexity of inflamed vessels compared with changes in blood volume or epidermal thickness. Measurements in eczema patients also captured changes in acanthosis, capillary-loop density and diameter, and vascular volume (Supplementary Fig. 3a–c), enabling the possibility of objective clinical evaluation of eczema severity or allergy testing over the ‘prick test’, which suffers from inter-observer variation²⁶.

In addition to a small, handheld form factor, portable UB-RSOM was shown to be insensitive to motion and capable of delivering high-resolution *in vivo* images of the skin within an acquisition time of around one minute. Therefore, even in this prototype format, UB-RSOM achieved scanning features appropriate for seamless integration in the dermatology suite. We expect that these features, along with the imaging depth, will lead to improved assessments of diseases and their treatments, thereby offering clinical value in dermatology examinations. FBE was employed to better visualize image features, in particular patterns associated with the high-frequency components. We employed different colours to represent the low- and high-frequency components to improve the contrast of the high-frequency part of the ultra-broad bandwidth. This representation allows for a quick appreciation of the information contained at high frequencies and ensures that high-frequency contrast is not masked by the low-frequency components, which are typically more intense. Future steps will include research into alternative image processing and representation schemes and further analysis of the implications of FBE and other methods for image contrast enhancement. FBE has a potential application in quantifying vasoconstriction and vasodilation. Regarding psoriasis management, a larger clinical study will allow refinement of the OPIND index and validation of its use as an accurate, quantitative and user-independent metric of psoriasis severity. UB-RSOM could be more broadly applied to the study and clinical evaluation of inflammatory skin diseases, hair, nevi, skin cancers and cardiovascular disease (see Supplementary Note 3). These measurements could be combined in the future with measurements of dermal infiltration by inflammatory cells, which could be achieved using optoacoustic contrast agents or through hybrid operation with confocal microscopy.

Adding the ability to take spectral measurements will be an important next step in the development of the portable UB-RSOM system. Operation at multiple wavelengths is currently limited by unavailability of portable ultra-fast pulsed lasers, achieving pulse widths of 1–3 ns at sufficient energy. Spectral RSOM imaging has been recently shown possible in healthy skin²⁷, but at a lower resolution and speed compared with those achieved here. This was due to employment of slow parametric oscillator lasers with pulse widths >10 ns, which are also bulky and very expensive for clinical use in dermatology. Progress in ultrafast laser technology is essential if spectral capacities are to be added to clinical UB-RSOM devices; this could enhance skin examinations by allowing measurement of oxygenation and differentiation of the melanin contributions.

Overall, the quantitative assessment of psoriatic and inflammatory biomarkers heralds new possibilities in the understanding of processes involved in the onset and progression of disease, as well as in the longitudinal monitoring of treatment options. UB-RSOM

has therefore the potential to enable quantitative and objective measurements of inflammatory landmarks.

Methods

Handheld UB-RSOM system. The UB-RSOM system that was developed is based on a custom-made spherically focused LiNbO₃ transducer constructed to yield broadband measurements ranging from 10 to 180 MHz (Fig. 1a). Typically, measurements were performed in the 10–180 MHz or 10–120 MHz bands. The 10–180 MHz band is important for resolving features below 15 µm, such as the capillary loops in healthy skin (Supplementary Note 2). The active element of the transducer has a diameter of 3 mm and a focal distance of 3 mm, leading to an f-number of 1. The detected optoacoustic signals are pre-amplified by a low noise amplifier (63 dB; AU-1291, Mited). The transducer scans perpendicular to its axial axis, conforming a rectangular grid parallel to the skin surface and keeping the focal point slightly above the skin surface.

In the scanning head, the transducer is attached to two motorized stages (size, 35 mm × 35 mm × 15 mm; Physik Instrumente). Illumination was delivered by a customized fibre bundle (CeramOptec) that ends in two arms (Supplementary Fig. 1a). At the bundle ends, individual fibres are arranged in a 6.5 mm × 2 mm rectangle (Fig. 1a) and illuminate a total surface of ~8 mm × 8 mm. Inside the illuminated surface a virtually homogeneous rectangular illumination pattern of 8 mm × 5 mm is achieved. The bundles are fixed to an ergonomic casing made via three-dimensional printing of acrylonitrile butadiene styrene. The illumination is generated by a 532 nm laser (Bright Solutions). The temporal width of the pulse is 0.9 ns and its maximum energy goes up to 1 mJ per pulse. The repetition rate can be selected from single shot up to 2 kHz. An articulated arm helps the user to fix the casing to the imaged area, minimizing motion artefacts in the reconstructed images (Fig. 1b,c). An interchangeable interface unit shielded with an optically and acoustically transparent plastic membrane is placed below the casing. The interface unit is filled with 1.5 ml of water and enables the acoustic coupling between the skin and the transducer detection surface. Once the unit is filled, the system is easily placed onto the desired skin area (Supplementary Fig. 1a). All psoriasis images were generated using optoacoustic signals collected over 4 mm × 2 mm (scan points, 266 × 135), taking a total time of 70 s. The entire patient handling process, including placement of the scanning head on the tissue surface lasted less than 2–3 min. A resolution and sensitivity characterization of the system is discussed in Supplementary Note 4.

Safety limits. According to the *American National Standard for Safe Use of Lasers*, when applying 532 nm light to a region for >10 s, the mean irradiance should not exceed 2,000 W m⁻². The measured energy per pulse and per area delivered to the sample was 3.75 µJ mm⁻², which imposes a maximum repetition rate of 533 Hz. To ensure safety we used a repetition rate of 500 Hz. Within this energy range, the temperature increase in the tissue is of the order of milliKelvin. Control measurements (not shown) demonstrated that there were no alterations in image appearance due to repeated scanning sessions, confirming the absence of UB-RSOM-induced temperature effects on skin physiology.

Image reconstruction, FBE and rendering. Data were collected using a raster-scan acquisition assuming an x–y plane parallel to the skin surface. At each position, several amplitude mode lines (‘A lines’) are obtained in the depth direction, that is, the z direction.

The acquired signals are divided into two frequency bands^{24,25}: 10–42 MHz (low) and 40–120 MHz (high) for the 10–120 MHz implementation. Alternatively, 10–60 MHz and 60–180 MHz bands were used for the 10–180 MHz implementation. Signals in the two different bands are independently reconstructed, a process necessary to reduce noise, especially in relation to reconstructing high-frequency data. Reconstructions are based on a beam-forming algorithm²⁸ that generates three-dimensional images. The beam-forming algorithm is accelerated by parallel computing on a graphics processing unit, and improved by incorporating the spatial sensitivity field of the detector as a weighting factor in the algorithm²⁹. The voxel size of the reconstruction grid was chosen to be 10 µm × 10 µm × 3 µm.

The two resulting images x_{low} and x_{high} correspond to the low- and high-frequency components of the signal (Fig. 1d,e). A weighting factor α is introduced for modulating the intensity of the high-frequency band image:

$$x_{high}^p = \alpha x_{high} \quad (1)$$

where x_{high}^p is the new high-frequency band image. A composite image (x_{RGB}) is then constructed by fusing x_{low} into the red channel of a red-green-blue (RGB) image and x_{high}^p into the green channel of the same RGB image (Fig. 1f–i). Then contrast between the red and green channel is maximized by solving the following minimization problem:

$$\min_{\alpha} \|x_{low} - \alpha x_{high}\|^2 \quad (2)$$

Representing α versus $\|x_{low} - \alpha x_{high}\|^2$ leads to a function with a clear parabolic shape whose minimum can be calculated simply by brute force minimum search (see Supplementary Note 1).

UB-RSOM images can then be rendered by taking the maximum intensity projections (MIPs) of the reconstructed images along the direction shown. In cross-sectional images, the entire volume is rendered. In coronal views, the MIP is shown from the reconstructed image within the limits of the layer shown along the z direction (depth).

Patient selection, skin biopsies, data grouping and general statistics. Thirteen psoriasis patients were imaged following approval from the Ethics Committee of the Klinik und Poliklinik für Dermatologie und Allergologie am Biederstein, Munich, Germany. Skin punch biopsies (6 mm diameter) from skin lesions and clinically non-involved skin were taken from all patients. Before obtaining biopsies, patients gave their written informed consent. Consent for publishing skin photos was also obtained (Fig. 2c,d). Biopsies were evaluated by an experienced pathologist to confirm the clinical diagnosis. CD31 immunostaining was also performed to evaluate vessel footprints.

The patients were split into two groups. Group A consisted of six patients whose mean age was 52. The data obtained from group A was used to evaluate UB-RSOM performance as shown in Fig. 2 and to find psoriasis biomarkers as shown in Fig. 3. To assess the significance of the statistical differences for the metrics used to compare healthy and adjacent psoriatic skin, we performed both a paired t -test and a Wilcoxon signed-rank test. Performing both tests ensured that the samples follow the required statistical distributions. For every metric, the variance between the healthy values and psoriatic values were of the same order. The selection of the healthy and psoriatic skin areas to be imaged was made by professional dermatologists, independently of the authors that processed the data.

Group A was also used to calculate the coefficients of the OPIND model. Group B consisted of eight psoriasis patients (mean age, 46) and was used to validate the OPIND performance. Details of these calculations and validation procedures are provided below in 'Calculation of OPIND'.

Two of the thirteen patients were excluded from the study since they moved during acquisition leading to reconstructions with pronounced artefacts.

Quantitative comparison between RSOM images and histological sections. To validate the UB-RSOM fidelity in relation to a gold standard, we compared the images obtained from healthy and psoriatic skin with corresponding histology samples. Values for epidermal thickness were determined at six equidistant points on the skin surface, in both the histological and the UB-RSOM images. We also measured the diameter of nine vessels in the psoriatic skin that were visualized by both UB-RSOM and CD31. The vessels were randomly selected.

Quantification of vascular and epidermal features in psoriatic patients. To quantify the skin features related to manifestation of psoriasis, we define the following grayscale image:

$$x_{\text{grey}} = x_{\text{low}} + x_{\text{high}}^p \quad (3)$$

The regions of the skin containing the features to be quantified are typically segmented from the image x_{RGB} , relying on the additional contrast provided by the FBE. Then the features are quantified in the corresponding regions of x_{grey} .

To calculate the TBV, fractal number and epidermal thickness, the distribution of the epidermal surface is first obtained using an in-house automatic segmentation algorithm. The images are then transformed (label, 't'), obtaining synthetic representations of the skin, x_{grey}^t and x_{RGB}^t , in which the epidermal surface is flat. In x_{RGB}^t the epidermis can be distinguished from the dermis (see Fig. 2a,b) due to the FBE. Both regions can be manually segmented by defining a plane parallel to the skin surface that splits the image into two cubes. The upper cube contains the epidermis and the lower cube contains the dermis (typically a volume of 4 mm × 2 mm × 2 mm was selected, although the dermis depth varied by patient). The height of the upper cube is taken as the epidermal thickness, and defines the maximum distance from the epidermal surface to the horizontal vascular plexus.

The image of the dermal microvasculature ($x_{\text{grey}}^{\text{tb}}$) is obtained by applying a binary mask (label, 'b') to the dermal region of the image x_{grey}^t , which sets to one the voxels whose value is above a threshold defined as 25% of the maximum voxel value, with the rest of the voxels being set to zero. The TBV is then calculated as $\text{TBV} = N \times dV$, where N is the number of nonzero voxels and dV is the voxel volume. The fractal number is obtained by applying the box counting method³⁰ to $x_{\text{grey}}^{\text{tb}}$.

The diameter and density of the elongated and dilated capillary loops was only calculated for the psoriatic skin. The calculation was performed using a coronal-view MIP of the epidermal regions of the image $x_{\text{high}}^{\text{pMIP}}$ (henceforth, $x_{\text{high}}^{\text{pMIP}}$), since it displays a map of the capillary loops (see Fig. 2c). First, the number of loops (n_{loop}) is determined by finding the number of connected components of pixels with a constant intensity value t , whose external boundary pixels all have a value less than t ; this also gives the density of the capillary loops. After applying a 10% threshold to $x_{\text{high}}^{\text{pMIP}}$, the mean area (A_{mean}) of the capillary-loop tips is calculated using the expression $A_{\text{mean}} = (N \times dV) / n_{\text{loop}}$ where N is the number of nonzero voxels. The diameter of the loops is then obtained, assuming that the area encompassed is a disc.

Calculation of OPIND. To further investigate the clinical relevance of UB-RSOM-resolved features we formulated the following severity index:

$$\text{OPIND} = a_1 + a_2 \text{ivasc} + a_3 \text{cdens} + a_4 \text{acanth} + a_5 \text{strucc} \quad (4)$$

where ivasc is the normalized increased vasculature (difference between the TBVs of psoriatic and adjacent healthy skin), cdens is the normalized capillary density, acanth is the normalized acanthosis (difference between the thicknesses of psoriatic and adjacent healthy skin) and strucc is the normalized structural change (difference between the fractal numbers of psoriatic and adjacent healthy skin). Using data group A, we observed a strong correlation between the PASI component 'erythema' and the ivasc (Pearson's correlation coefficient, 0.86) where corr is the Pearson's correlation coefficient. We also observed that the acanth values matched the PASI 'induration' value, as estimated by a licensed dermatologist. However, low correlation was observed between other PASI components and OPIND components. For this reason, we assigned $a_3 = a_5 = 0$.

Using the data from Group A as a training set, we calculated the values of a_1 , a_2 and a_4 via linear regression to the following expression:

$$\text{PASI} = a_1 + a_2 \text{ivasc} + a_4 \text{acanth} \quad (5)$$

The PASI index was calculated by summing the 'erythema' and the 'induration' values. We obtained $a_2 = 2.29$ (standard error, 0.81; $P < 0.05$), $a_4 = 1.81$ (standard error, 0.3; $P < 0.01$) and $a_1 = 0.00$ ($P < 0.001$). For pilot validation of the generality of the OPIND index, calculated on the basis of the computed a_1 , a_2 and a_4 values, we calculated the OPIND values for the patients included in group B (as shown in Fig. 3e). We calculated the percentage of the PASI variance that was explained by the OPIND index.

Code availability. Custom code is available in Github at <https://github.com/juanaguir/UB-RSOM>.

Data availability. The authors declare that all data supporting the findings of this study are available within the paper and its Supplementary Information. Raw acquired optoacoustic data can be made available upon reasonable request, with permission of the Klinik und Poliklinik für Dermatologie und Allergologie am Biederstein, Munich, Germany.

Received 1 September 2016; accepted 29 March 2017;
published 10 May 2017

References

- Nestle, F. O., Kaplan, D. H. & Barker, J. Psoriasis. *N. Engl. J. Med.* **361**, 496–509 (2009).
- Horn, E. J. *et al.* Association of patient-reported psoriasis severity with income and employment. *J. Am. Acad. Dermatol.* **57**, 963–971 (2007).
- Boehncke, W. H. & Schon, M. P. Psoriasis. *Lancet* **386**, 983–994 (2015).
- Griffiths, C. E. & Barker, J. N. Pathogenesis and clinical features of psoriasis. *Lancet* **370**, 263–271 (2007).
- Oji, V. & Luger, T. A. The skin in psoriasis: assessment and challenges. *Clin. Exp. Rheumatol.* **33**, S14–S19 (2015).
- Ashcroft, D. M., Wan Po, A. L., Williams, H. C. & Griffiths, C. E. Clinical measures of disease severity and outcome in psoriasis: a critical appraisal of their quality. *Br. J. Dermatol.* **141**, 185–191 (1999).
- Marks, R. Measurement of the response to treatment in psoriasis. *J. Dermatolog. Treat.* **7**, S7–S10 (1996).
- Ryan, C. *et al.* Research gaps in psoriasis: opportunities for future studies. *J. Am. Acad. Dermatol.* **70**, 146–167 (2014).
- Lacarrubba, F., Pellacani, G., Gurgone, S., Verzi, A. E. & Micali, G. Advances in non-invasive techniques as aids to the diagnosis and monitoring of therapeutic response in plaque psoriasis: a review. *Int. J. Dermatol.* **54**, 626–634 (2015).
- Archid, R. *et al.* Confocal laser-scanning microscopy of capillaries in normal and psoriatic skin. *J. Biomed. Opt.* **17**, 101511 (2012).
- Alex, A. *et al.* Multispectral *in vivo* three-dimensional optical coherence tomography of human skin. *J. Biomed. Opt.* **15**, 026025 (2010).
- Pan, Y. & Farkas, D. L. Noninvasive imaging of living human skin with dual-wavelength optical coherence tomography in two and three dimensions. *J. Biomed. Opt.* **3**, 446–455 (1998).
- Zabihian, B. *et al.* *In vivo* dual-modality photoacoustic and optical coherence tomography imaging of human dermatological pathologies. *Biomed. Opt. Express* **6**, 3163–3178 (2015).
- Blatter, C. *et al.* *In situ* structural and microangiographic assessment of human skin lesions with high-speed OCT. *Biomed. Opt. Express* **3**, 2636–2646 (2012).
- Qin, J., Jiang, J., An, L., Gareau, D. & Wang, R. K. *In vivo* volumetric imaging of microcirculation within human skin under psoriatic conditions using optical microangiography. *Lasers Surg. Med.* **43**, 122–129 (2011).
- Errico, C. *et al.* Ultrafast ultrasound localization microscopy for deep super-resolution vascular imaging. *Nature* **527**, 499–502 (2015).

17. Gutierrez, M. *et al.* High-frequency sonography in the evaluation of psoriasis: nail and skin involvement. *J. Ultrasound. Med.* **28**, 1569–1574 (2009).
18. Jetzfellner, T. *et al.* Optoacoustic tomography with varying illumination and non-uniform detection patterns. *J. Opt. Soc. Am.* **27**, 2488–2495 (2010).
19. Mancardi, D., Varetto, G., Bucci, E., Maniero, F. & Guiot, C. Fractal parameters and vascular networks: facts and artifacts. *Theor. Biol. Med. Model.* **5**, 12 (2008).
20. Favazza, C. P., Jassim, O., Cornelius, L. A. & Wang, L. V. *In vivo* photoacoustic microscopy of human cutaneous microvasculature and a nevus. *J. Biomed. Opt.* **16**, 016015 (2011).
21. Braverman, I. M. & Keh-Yen, A. Ultrastructure of the human dermal microcirculation. III. The vessels in the mid- and lower dermis and subcutaneous fat. *J. Invest. Dermatol.* **77**, 297–304 (1981).
22. Aguirre, J. *et al.* Broadband mesoscopic optoacoustic tomography reveals skin layers. *Opt. Lett.* **39**, 6297–6300 (2014).
23. Schwarz, M., Omar, M., Buehler, A., Aguirre, J. & Ntziachristos, V. Implications of ultrasound frequency in optoacoustic mesoscopy of the skin. *IEEE Trans. Med. Imaging* **34**, 672–677 (2014).
24. Omar, M., Soliman, D., Gateau, J. & Ntziachristos, V. Ultrawideband reflection-mode optoacoustic mesoscopy. *Opt. Lett.* **39**, 3911–3914 (2014).
25. Omar, M., Schwarz, M., Soliman, D., Symvoulidis, P. & Ntziachristos, V. Pushing the optical imaging limits of cancer with multi-frequency-band raster-scan optoacoustic mesoscopy (RSOM). *Neoplasia* **17**, 208–214 (2015).
26. Verstege, A. *et al.* The predictive value of the skin prick test weal size for the outcome of oral food challenges. *Clin. Exp. Allergy* **35**, 1220–1226 (2005).
27. Schwarz, M., Buehler, A., Aguirre, J. & Ntziachristos, V. Three-dimensional multispectral optoacoustic mesoscopy reveals melanin and blood oxygenation in human skin *in vivo*. *J. Biophotonics* **9**, 55–60 (2015).
28. Omar, M., Gateau, J. & Ntziachristos, V. Raster-scan optoacoustic mesoscopy in the 25–125 MHz range. *Opt. Lett.* **38**, 2472–2474 (2013).
29. Turner, J., Estrada, H., Kneipp, M. & Razansky, D. Improved optoacoustic microscopy through three-dimensional spatial impulse response synthetic aperture focusing technique. *Opt. Lett.* **39**, 3390–3393 (2014).
30. Foroutan-pour, K., Dutilleul, P. & Smith, D. L. Advances in the implementation of the box-counting method of fractal dimension estimation. *Appl. Math. Comput.* **105**, 15 (1999).

Acknowledgements

We acknowledge funding from European Grant INNODERM (687866) Horizon 2020 and Deutsche Forschungsgemeinschaft, Germany (Leibniz Prize 2013; NT 3/10-1).

Author contributions

J.A. designed and developed the imaging system, designed and performed the experiments, processed the data, provided conceptual input and wrote the paper. M.S. developed the imaging system, performed the experiments, processed the data. N.G. provided conceptual input and performed the histology experiments. M.O. developed the imaging system and performed the characterization experiments. A.B. provided conceptual input. K.E. provided conceptual input and designed the experiments. V.N. provided conceptual input, designed the experiments, supervised and led the research, and wrote the paper. J.A., M.S., M.O., A.B. and V.N. revised the text after the referees' comments.

Additional information

Supplementary information is available for this paper.

Reprints and permissions information is available at www.nature.com/reprints.

Correspondence and requests for materials should be addressed to V.N.

How to cite this article: Aguirre, J. *et al.* Precision assessment of label-free psoriasis biomarkers with ultra-broadband optoacoustic mesoscopy. *Nat. Biomed. Eng.* **1**, 0068 (2017).

Publisher's note: Springer Nature remains neutral with regard to jurisdictional claims in published maps and institutional affiliations.

Competing interests

V.N. is a shareholder in iThera-Medical GmbH, Munich, Germany.